PROCEEDINGS OF THE ROYAL SOCIETY A
FirstCite® e-publishing

Proc. R. Soc. A
doi:10.1098/rspa.2006.1758
Published online

The Hide, Skeldon, Acheson dynamo revisited

By Irene M. Moroz*

Mathematical Institute, 24-29 St Giles', Oxford OX1 3LB, UK

Hide *et al.* (Hide, Skeldon & Acheson 1996 *Proc. R. Soc. A* **452**, 1369–1395) introduced a nonlinear system of three coupled ordinary differential equations to model a self-exciting Faraday disk homopolar dynamo. A very small selection of its possible behaviours was presented in that paper. Subsequent studies have extended the system to incorporate the effects of a nonlinear motor, an external battery and magnetic field, the coupling of two or more identical dynamos together, among other things. In this paper, we return to the original model with a view to perform a more extensive analysis of the Hide *et al.* dynamo. For the first time, we present bifurcation transition diagrams, so that the two examples of chaotic dynamo action (shown in figure 9 in that paper) can now be placed into context. We exhibit the coexistence of multiple attractors and also identify the lowest order unstable periodic orbits pertaining to some specific cases.

Keywords: unstable periodic orbits; dynamo models; bifurcations

1. Introduction

Hide *et al.* (1996; hereafter denoted as HSA) introduced the following system of three dimensionless nonlinear coupled ordinary differential equations to model a self-exciting Faraday disk homopolar dynamo,

$$\dot{x} = x(\tilde{y}-1)-\beta z, \tag{1.1a}$$

$$\dot{\tilde{y}} = \alpha(1-x^2)-\kappa\tilde{y}, \tag{1.1b}$$

$$\dot{z} = x-\lambda z. \tag{1.1c}$$

Here, $x(t)$ is the current flowing through the dynamo, $\tilde{y}(t)$, the angular rotation rate of the disk and $z(t)$, the angular rotation rate of the motor (see eqns (2.13) and (2.14) of HSA). The system (1.1) contains four positive parameters. κ and λ are the coefficients of friction in the disk and the motor, respectively. The parameter α is proportional to the steady applied mechanical couple, driving the disk into rotation, while β^{-1} measures the moment of inertia of the armature of the motor. We also find it convenient to work with the parameter combinations $\bar{\alpha}=\alpha/\kappa$ and $\bar{\beta}=\beta/\lambda$.

HSA remark that the original motivation behind their investigations was a simple dynamo analogue for the heat-storage capacity in the oceans, considered to be an important factor in the dynamical processes underlying the El Niño Southern Oscillation. They also note that the equivalence of a capacitor to a motor as a circuit element opened up the relevance to the geomagnetic field.

*moroz@maths.ox.ac.uk

Received 2 March 2006
Accepted 28 June 2006

The HSA dynamo was observed to exhibit steady, regular and irregular solutions, provided $\bar{\alpha}$ exceeded a critical value, depending upon both β and λ. The controlling centre for the bifurcations is a codimension-two Takens–Bogdanov double-zero bifurcation in the (β, α)-parameter space (see HSA and below for details). This bifurcation is degenerate here in the sense that all the three equilibrium states undergo multiple bifurcation at the same point in parameter space.

Building upon new sets of nonlinear ordinary differential equations, which govern a wide range of novel single and coupled dynamo systems formulated by Hide (1997*a*,*b*), as extentions of the HSA system, Moroz *et al.* (1998), Goldbrum *et al.* (2000) and Moroz (2001*a*,*b*, 2002) have analysed aspects of the influence on the HSA system of nonlinearity of the series motor, the presence of a series battery and/or an ambient magnetic field. While these extensions can be viewed as toy dynamo models in their own right, Hide (1997*b*) comments upon their geophysical and astrophysical significance, providing, for example in Moroz (2001*a*), a metaphor for the geodynamo immersed in the background solar magnetic field. The nonlinear series motor, proposed by Hide (1997*a*) to study the quenching of oscillatory dynamo action in the original HSA model, arises when a nonlinear torque is applied to the armature of the electric motor. The reader is referred to Hide (1997*a*) for further details.

The inclusion of some of these extra effects has succeeded in separating the multiple double-zero bifurcation, creating additional steady-state bifurcation curves as well as codimension-two Hopf-zero bifurcations.

In the original HSA study, only a very small selection of all the possible behaviours was investigated, some of which represented unlikely choices of the parameters. In this paper, we return to the original HSA model with a view to present a more complete picture of the dynamo, by placing the two examples of chaotic behaviour shown in figure 9 in that paper in context by means of bifurcation transition diagrams. By doing so, we hope ultimately to be able to identify those additional features, which arise in the extensions to the HSA dynamo as reported earlier.

There has been considerable interest in recent years in characterizing chaotic attractors of nonlinear dynamical systems, such as the Lorenz equations, in terms of the spectrum of unstable periodic orbits (UPOs), determined from time-series. While a chaotic attractor possesses an infinite number of UPOs, it is believed that many properties may be determined from those orbits of lowest period.

One approach, developed by Cvitanovic and his co-workers (e.g. Artuso *et al.* 1990*a*,*b*), enables the statistical properties of the underlying chaotic attractor to be expressed as weighted sums over the UPOs. Another approach, followed by Gilmore and his collaborators (e.g. Gilmore 1998; Gilmore & Lefranc 2002) is to identify the basic template of an attractor and the ordering of UPOs, from knowledge of topological invariants, such as the linking number, the local torsion and the twist, using the lowest order UPOs. It is this second approach that provides the motivation and long-term goal of our research, of which the work presented here is the starting point for the HSA dynamo.

In a recent study, Moroz (2005*a*) investigated what happened to the lowest order UPOs of the extended Malkus–Robbins (hereafter denoted as EMR) dynamo as the dimensionless parameter β is increased from 0 (the limit which yields the celebrated Lorenz equations) to the loss of chaotic motion to either steady or periodic dynamo action. The classic Lorenz parameter choices of $r=28$,

$\sigma=10$ and $b=8/3$ were used for two of the cases considered in Moroz (2003, 2004). A subsequent paper (Moroz 2005*b*) has extended the study to the remaining two cases of interest in Moroz (2003).

Therefore, in addition to producing bifurcation diagrams for some of the non-degenerate limits of the HSA dynamo, we present preliminary investigations of the lowest order UPOs for selected parameter values, adopting the same procedures as used for the EMR dynamo.

The paper is structured as follows. In §2, we review the relevant aspects of the HSA dynamo, recasting it in a different form that is more convenient for the subsequent analysis. In §3, we present some bifurcation transition diagrams and in §4, we focus upon some specific parameter choices, demonstrating the coexistence of multiple attractors, presenting first return maps and identifying stable and unstable periodic orbits from time-series calculations for selected parameter values. We discuss our results and indicate the future directions for study in §5.

2. The Faraday disk dynamo

Introducing $y(t)=\bar{\alpha}-\tilde{y}(t)$, equation (1.1) becomes,

$$\dot{x} = (\bar{\alpha}-1)x - xy - \bar{\beta}\lambda z, \tag{2.1a}$$

$$\dot{y} = \kappa(\bar{\alpha}x^2 - y), \tag{2.1b}$$

$$\dot{z} = x - \lambda z. \tag{2.1c}$$

The interested reader is referred to the original HSA paper for complete details of the derivation of these equations.

(*a*) *Review of the linear stability analysis*

Equations (2.1) possess three equilibrium solutions,

$$\boldsymbol{x}_0 = (x_0, y_0, z_0) = (0,0,0), \tag{2.2}$$

which we term the trivial equilibrium and

$$\boldsymbol{x}_\mathrm{e} = (x_\mathrm{e}, y_\mathrm{e}, z_\mathrm{e}) = (x_\mathrm{e}, \bar{\alpha}x_\mathrm{e}^2, x_\mathrm{e}/\lambda), \tag{2.3}$$

where $x_\mathrm{e}=\pm[1-(1+\bar{\beta})/\bar{\alpha}]^{1/2}$, which we term the non-trivial equilibria. HSA consider examples in which $\lambda=0$. In our study, we confine our interests to non-zero values of both λ and κ, and express bifurcations in the $(\bar{\beta},\bar{\alpha})$-plane.

The trivial equilibrium undergoes a pitchfork bifurcation along the line

$$\bar{\alpha}_\mathrm{s} = 1 + \bar{\beta}, \tag{2.4}$$

corresponding to $x_\mathrm{e}=0$ in equation (2.3), thereby creating the two non-trivial equilibrium states. A supercritical Hopf bifurcation occurs on

$$\bar{\alpha}_\mathrm{h} = 1 + \lambda. \tag{2.5}$$

The non-trivial equilibria undergo subcritical Hopf bifurcations on

$$\bar{\alpha}_\mathrm{H} = 1 + \frac{3}{2}\bar{\beta} + \frac{\lambda[2\bar{\beta}-(\kappa+\lambda)]}{2(\kappa-\bar{\beta})}, \tag{2.6}$$

provided

$$\bar{\alpha} + \lambda/2 > 3\bar{\beta}/2 + 1,$$

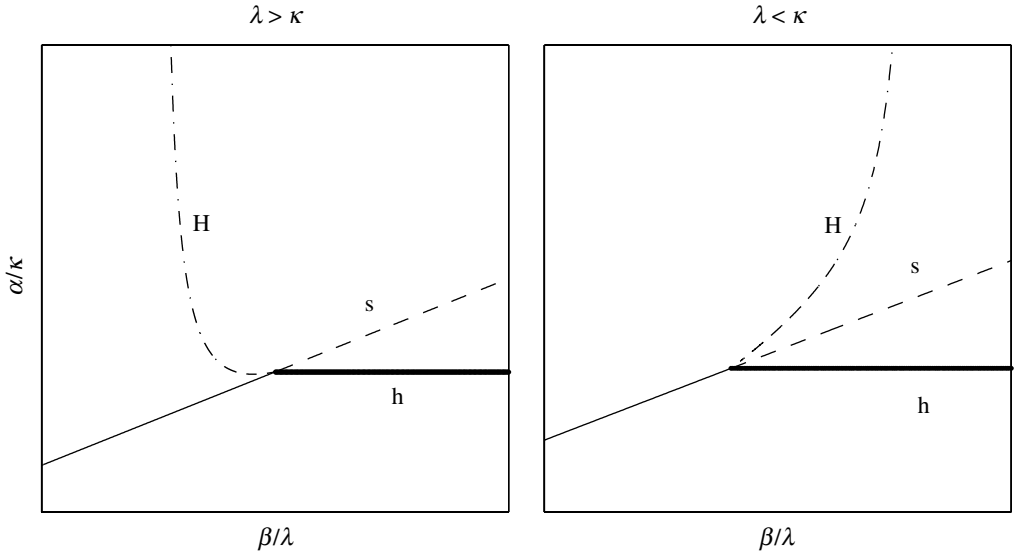

Figure 1. Typical linear stability curves for the HSA dynamo for $\lambda > \kappa$ and $\lambda < \kappa$. s denotes the steady bifurcation curve, solid for stable and dashed for unstable; h denotes the Hopf bifurcation curve for the trivial equilibrium state; and H for the non-trivial equilibria.

and $\bar{\beta} \neq \kappa$. In addition, all the three equilibria undergo a codimension-two double-zero bifurcation at the point $(\bar{\beta}, \bar{\alpha}) = (\lambda, 1 + \lambda)$.

From equation (2.6), we see that $\bar{\alpha}_{\mathrm{H}} \to \infty$ as $\bar{\beta} \to \kappa$, which means that the double-zero bifurcation point falls to the right of this vertical asymptote whenever $\lambda > \kappa$ and to the left when this inequality is reversed.

Figure 1 shows the linear stability curves for both of these cases. Note that the parameter choice made by HSA for figure 9*b* in their paper has the double-zero and vertical asymptote coinciding. In our study, we shall also present results for $\kappa \neq \lambda$. The linear stability curves shown in figure 5 of HSA are a typical scenario for $\lambda > \kappa$.

(*b*) *The Poincaré section*

Following the procedure described by Koga (1986) for constructing a Poincaré section for the Lorenz equations by translating the z variable by its non-trivial equilibrium state value, we introduce $Y = y - \bar{\alpha} x_{\mathrm{e}}^2$. Equations (2.1) then become

$$\dot{x} = \left(\bar{\alpha} - 1 - \bar{\alpha} x_{\mathrm{e}}^2\right) x - xY - \bar{\beta}\lambda z, \tag{2.7a}$$

$$\dot{Y} = \kappa(\bar{\alpha} x^2 - Y - \bar{\alpha} x_{\mathrm{e}}^2), \tag{2.7b}$$

$$\dot{z} = x - \lambda z, \tag{2.7c}$$

with equilibria at

$$(x_0, Y_0, z_0) = (0, -\bar{\alpha} x_{\mathrm{e}}^2, 0), \qquad (x_{\mathrm{e}}, Y_{\mathrm{e}}, z_{\mathrm{e}}) = (x_{\mathrm{e}}, 0, x_{\mathrm{e}}/\lambda). \tag{2.8}$$

The Poincaré section is then taken to be

$$\mathcal{S} = \{(x, z) : Y = 0,\ \dot{Y} > 0,\ x > 0\}. \tag{2.9}$$

3. Bifurcation transition curves

Figure 9 of HSA displays chaotic behaviour for two different sets of parameter values: $(\alpha, \beta, \kappa, \lambda) = (20.0, 2.0, 1.0, 1.2)$ and $(\alpha, \beta, \kappa, \lambda) = (100.0, 1.01, 1.0, 1.0)$. In the former case, the number of oscillations around one of the non-trivial equilibria prior to reversal was small compared to the latter case. These results were presented as isolated integrations, with no indication of what the neighbouring dynamics might be. In this section, we rectify this by presenting for the first time bifurcation transition diagrams, appropriate for these two examples as well as for other choices in which $\kappa \neq \lambda$. In addition, we illustrate the effects of hysteresis on the transition sequence. Such plots will guide our calculations, enabling us to identify the lowest order UPOs responsible for generating the time-series, and to see how they evolve as parameters vary. In this paper, we shall focus upon presenting results for the two choices of α selected by HSA for their figure 9, beginning with $\alpha = 20$.

(*a*) $\alpha = 20$

Figure 2 shows the bifurcation transition diagrams for $\alpha = 20$, $\lambda = 1.2$ and $\kappa = 1.0$, while figure 3 shows the corresponding diagrams for $\lambda = 1.0$ and $\kappa = 1.2$. Two plots are shown in each case, demonstrating the consequences of hysteresis. These plots were constructed by integrating equation (2.7*a*–*c*) with a time-step of 0.01 s for 300 s, and recording the maximum value of Y for a particular choice of β, after transients have been allowed to decay. The final values of (x, Y, z) in one run were then taken to be the initial conditions for the next run for the next increment/decrement in β, taken as 0.015.

HSA's choice of $\beta = 2.0$ and $\lambda = 1.2$ gives $\bar{\beta} \approx 1.66667$ and corresponds to a value well inside the chaotic regime, according to figure 2. The sudden onset of irregular behaviour for small values of $\bar{\beta}$ from a steady state, and the subsequent loss to periodic solutions, are both subject to hysteresis. The loss to steady states is associated with the subcritical Hopf bifurcation (the curve, labelled as H in figure 1), which the non-trivial equilibria of equation (2.8) undergo. Hysteresis is a common feature of such subcritical bifurcations. The loss to periodic solutions is through intermittent destabilization of the regular periodic behaviour with irregular bursts. When $\bar{\beta}$ is increased, the transition from steady-state solutions occurs for $\bar{\beta} \approx 1.05$, while the onset of periodic solutions occurs for $\bar{\beta} \approx 2.2$. When $\bar{\beta}$ is decreased, the corresponding values are $\bar{\beta} \approx 0.94$ and $\bar{\beta} \approx 2.15$, respectively.

Figure 3 represents a case not considered by HSA, but which provides an even more dramatic example of hysteresis for larger values of $\bar{\beta}$. When $\bar{\beta}$ is increased, the onset of oscillatory states occurs for $\bar{\beta} \approx 1.24$, and the loss to sustained periodic solutions at $\bar{\beta} \approx 2.3$. When $\bar{\beta}$ is decreased, these transitions occur at $\bar{\beta} \approx 1.15$ and $\bar{\beta} \approx 2.45$, respectively. Hence, we find the coexistence of regular and irregular states as well as different regular solutions.

(*b*) $\alpha = 100$

When $\alpha = 100$, figure 9*b* of HSA shows that many more oscillations occur in the time-series for the x variable before a reversal occurs. HSA chose the value of $\beta = 1.01$ for their plots. From either of the two bifurcation diagrams in figure 4,

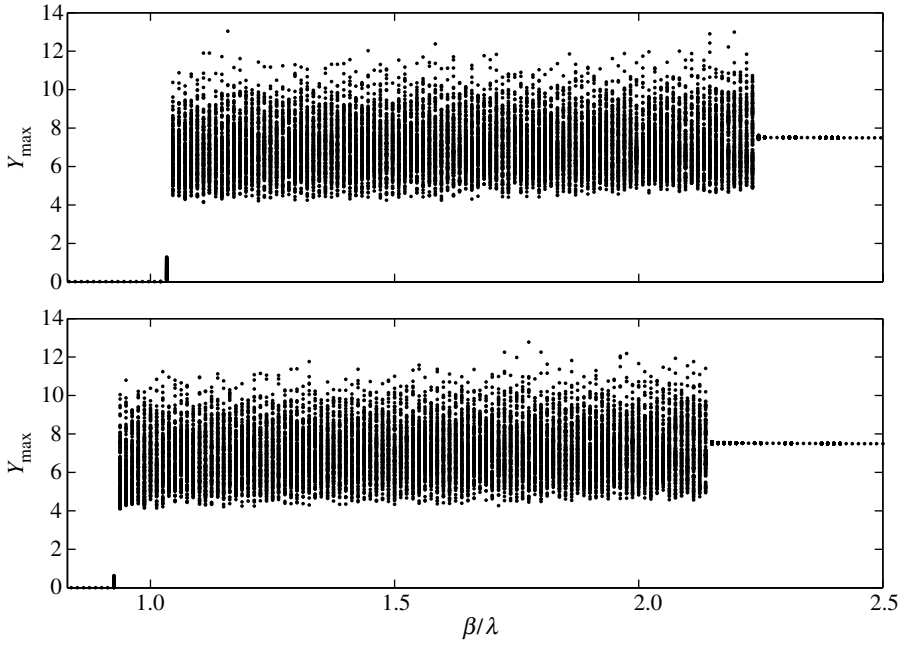

Figure 2. Bifurcation transition diagrams, as functions of $\bar{\beta}$ for $\alpha=20$, $\lambda=1.2$ and $\kappa=1.0$. The upper plot is for β increasing, while the lower is for β decreasing. Hysteresis occurs at both ends of the irregular regime.

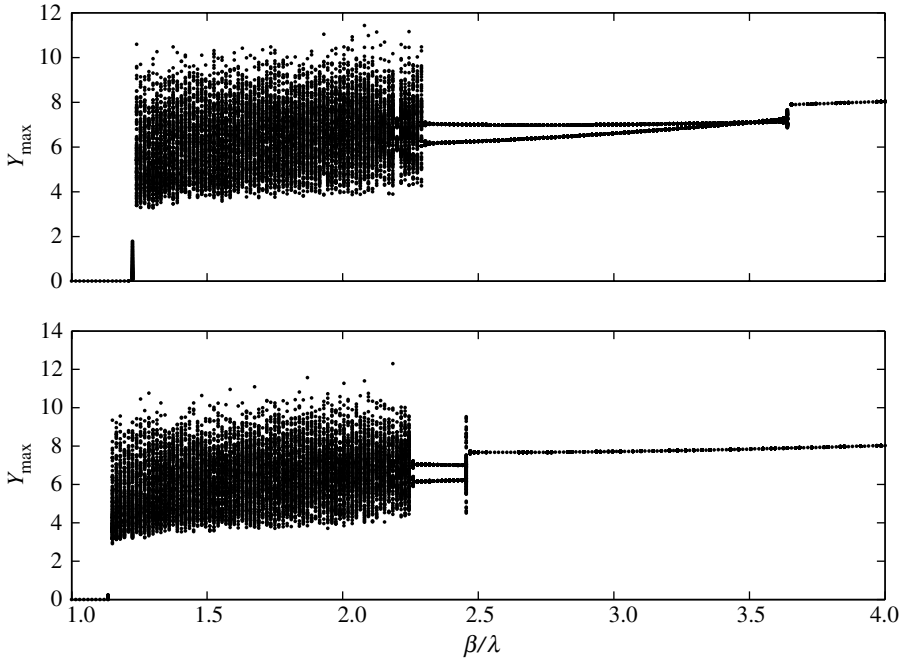

Figure 3. Bifurcation transition diagrams, as functions of $\bar{\beta}$ for $\alpha=20$, $\lambda=1.0$ and $\kappa=1.2$. The upper plot is for β increasing, while the lower is for β decreasing. Hysteresis again occurs.

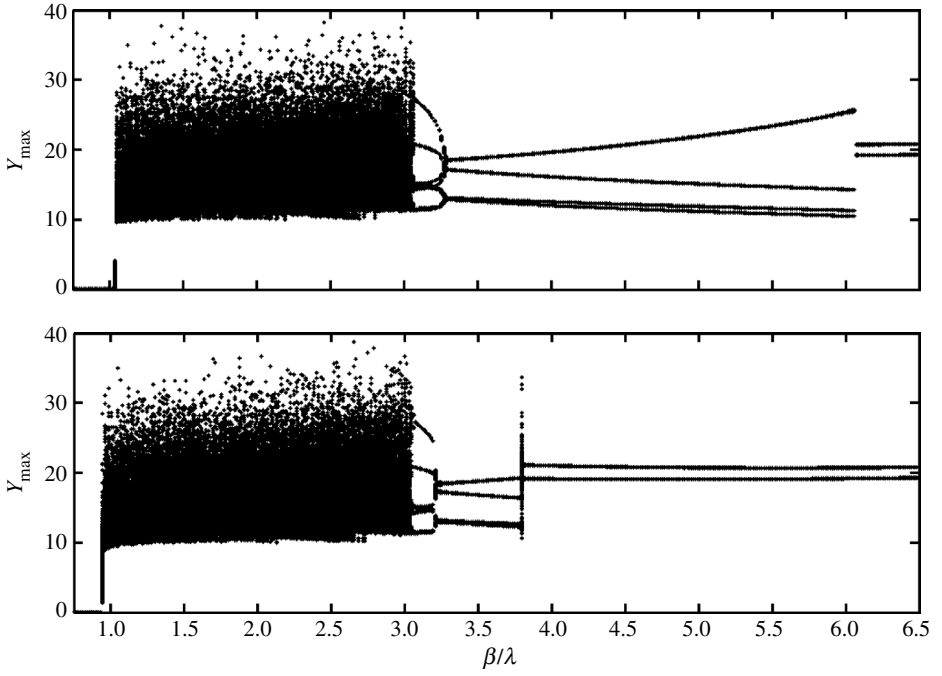

Figure 4. The bifurcation transition diagrams, corresponding to figure 9*b* of HSA, as $\bar{\beta}$ varies for $\alpha=100$, $\lambda=1.0$ and $\kappa=1.0$. The upper plot is for β increasing, while the lower is for β decreasing.

we see that such a choice falls close to the loss of stability of the oscillations to steady dynamo action. As we shall see later, the number of oscillations prior to reversal decreases markedly as β increases. Since, the choice of $\lambda=\kappa$ corresponds to the double-zero bifurcation coinciding with the vertical asymptote for the subcritical Hopf bifurcation, we decided to investigate non-degenerate choices of λ and κ, selecting the same values as for the $\alpha=20$ problem.

Figure 5 shows the bifurcation transition sequences for $\lambda=1.0$ and $\kappa=1.2$, while figure 6 shows the corresponding plots for $\lambda=1.2$ and $\kappa=1.0$.

The hysteresis is again evident within both the chaotic and the periodic regimes, leading to coexisting steady and chaotic states, periodic and chaotic states, as well as different types of periodic states. We return to examples of this in §4. Figure 6 shows that the numerical integrations for $\alpha=100$ also contain windows of simple periodic solutions within the chaotic regions. In each of these three examples, the extent of the chaotic region and its subsequent loss of stability to stable periodic states are larger than for the $\alpha=20$ cases.

4. Numerical integrations

Having presented a selection of the bifurcation transition curves, appropriate for figure 9 of HSA, we turn our attention to the numerical integrations for specific choices of α and β, beginning with some examples of stable periodic solutions and hysteresis.

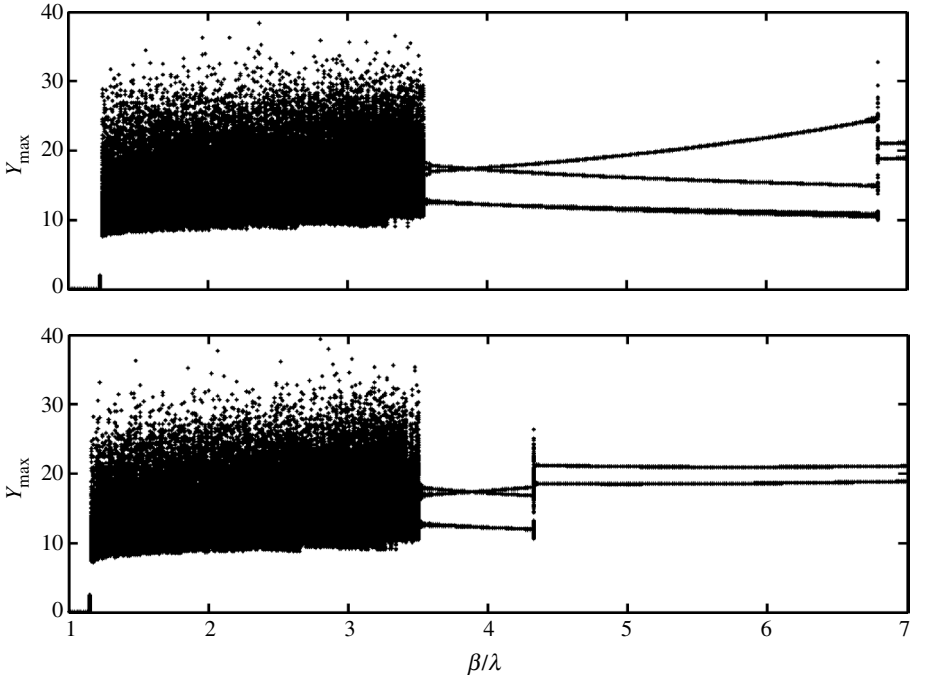

Figure 5. The bifurcation transition diagrams for $\alpha=100$, $\lambda=1.0$ and $\kappa=1.2$. The upper plot is for β increasing, while the lower is for β decreasing.

(*a*) *Periodic solutions and hysteresis*

Guided by the signs of the non-trivial equilibria, we shall adopt the standard protocol of labelling trajectories using symbol sequences R_n if the trajectory cycles n times around the equilibrium $x_e>0$, and L_m if the trajectory cycles m times around the negative equilibrium $x_e<0$. Each symbol L or R will be taken to correspond to one period. Thus, for example, RL, which cycles once around each equilibrium state, would be a period-2 solution.

Figure 7 shows examples of the coexistence of stable periodic orbits for $\alpha=100$ and $\lambda=\kappa=1$ (see figure 4). We show in the top and the bottom pairs of plots in figure 7, two different periodic solutions which can exist for $\beta=4$, depending upon whether β is increased (a period-8 R_4L_4 cycle) or decreased (a period-6 R_3L_3 cycle). When $\beta=8$, we found the stable periodic R_3L_3 state (see middle pair of figure 7) for both β increasing and decreasing.

Figure 8 shows a selection of stable periodic solutions found for $\alpha=100$, $\lambda=1.2$ and $\kappa=1$ when β is decreased, including one example of a period-doubled R_4L_4 orbit with period 8.4836 s for $\beta=3.54$ ($\bar{\beta}=2.95$), which falls within a periodic window of figure 6. Also shown are a period-6 R_3L_3 orbit with period 3.1503 s for $\beta=4.2$ ($\bar{\beta}=3.5$) and a period-4 R_2L_2 orbit with period 2.182 s for $\beta=4.8$ ($\bar{\beta}=4$). Figure 6 indicates that when $\bar{\beta}=4.5$, the period-8 cycle R_4L_4 for β increasing (not shown here) has been lost, leaving the period-4 R_2L_2 cycle with period 3.0573 s as the observed periodic behaviour in both β increasing and decreasing cases.

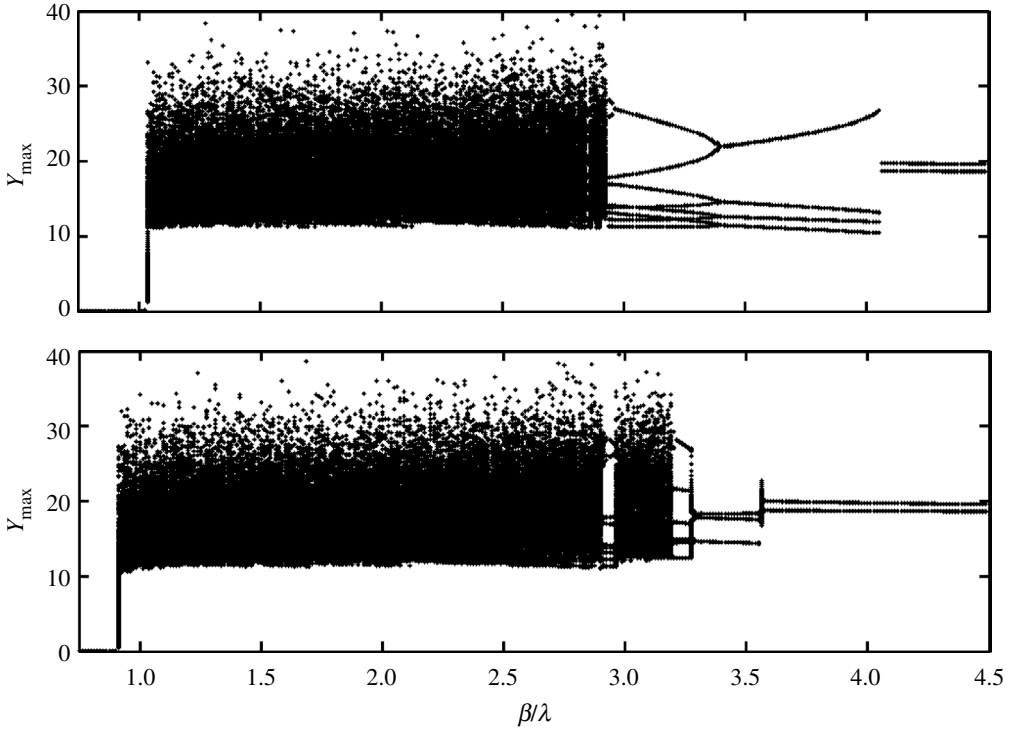

Figure 6. The bifurcation transition diagrams for $\alpha=100$, $\lambda=1.2$ and $\kappa=1.0$. The upper plot is for β increasing, while the lower is for β decreasing.

(*b*) *Unstable periodic orbits*

In addition to stable periodic solutions found in windows between and at the end of chaotic regimes, we also determined the dominant UPOs that contributed to the chaotic solutions of the HSA dynamo.

As with the EMR dynamo, to determine the close returns we integrated equation (2.7*a–c*) for 60 000 s using a time-step of 0.001 s, discarding the first 100 s as representing transients. The selection of a close return on the Poincaré section was accomplished using the criterion

$$\| \boldsymbol{Y}_i - \boldsymbol{Y}_j \| < \epsilon,$$

where $\boldsymbol{Y}_m=(x_m, Y_m, z_m)$ and $m=i, j$ denote the ith and jth intersections. We chose $\epsilon=0.005$ to define the ball of close returns in nearly all cases. The exception being for figure 13, where the two upper plots were obtained for $\epsilon=0.015$, in order to illustrate a rare example of an L_3R_3 periodic orbit.

We were able to guarantee that the trajectories landed precisely upon the Poincaré section, regardless of the size of the integration step, by adopting the approach described in Hénon (1982). This is achieved by rewriting the HSA equations with Y as the independent variable instead of t and integrating the resulting equations for one step from Y_a to $Y=0$. Here, t_a is the time just before Y changes sign.

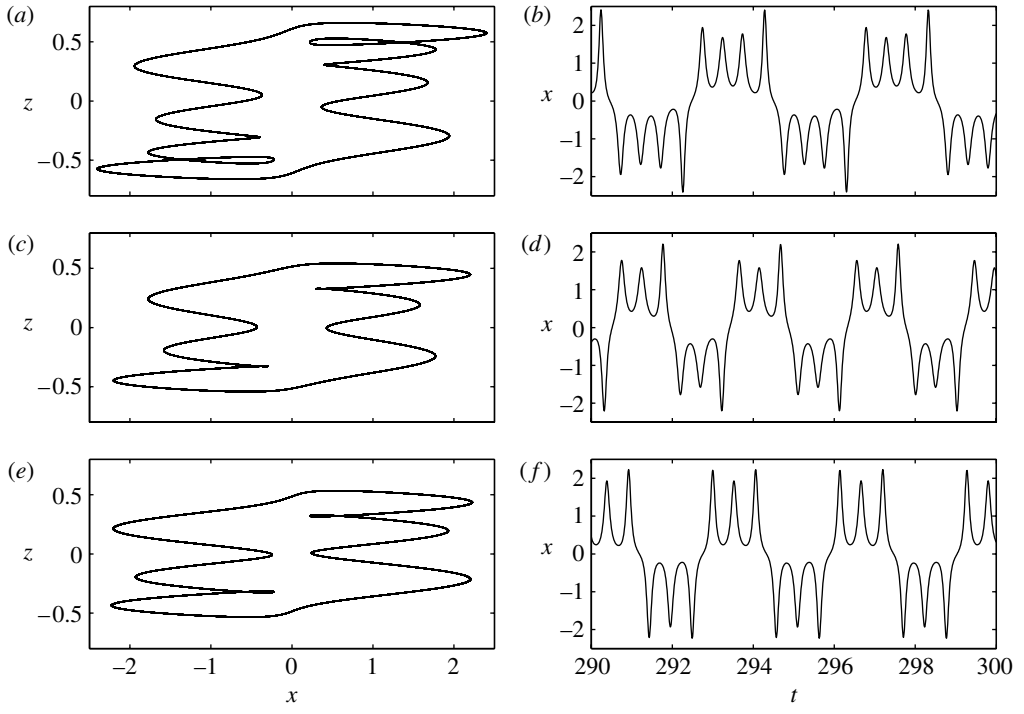

Figure 7. Phase portraits and time-series for $\alpha=100$, $\lambda=1.0$ and $\kappa=1.0$. Plots (a) and (b) $\beta=4$, β increasing; (c) and (d) $\beta=8$, β increasing or decreasing; and (e) and (f) $\beta=4$, β decreasing.

We also computed first return maps, based upon successive maxima of Y by analogy with the Lorenz equations (Lorenz 1963), in which successive maxima of z were plotted by integrating the HSA equations for 60 000 s with a time-step of 0.001 s.

(c) $\alpha=20$

Figure 9 shows a selection of the time-series and the phase portraits for the HSA dynamo when $\alpha=20$, $\beta=2$, $\lambda=1.2$ and $\kappa=1.0$. This corresponds to figure 9a of HSA. We include this for completeness and for ease of comparison with the UPO plots. We demonstrate the coexisting basins of attraction as a result of the reflectional symmetry of the HSA dynamo in figure 10, which shows the phase portraits in the (x, z)-plane and the time-series of $x(t)$ for two different initial conditions (x, y, z) and $(-x, y, -z)$, integrated over a longer time-interval than for the case in figure 9. These projections show that one of the attractors is the rotated image of the other.

Figure 11 shows the first return maps as plots of successive maximum values of Y when $\alpha=20$ and $\beta=2$. Figure 11a shows the results for $\lambda=1.2$ and $\kappa=1$ and figure 11b those for $\lambda=1$ and $\kappa=1.2$. For comparison purposes, we include as figure 11c, the familiar first return map of z_n versus z_{n+1} for the Lorenz equations with the classic parameter choice of $r=28$, $\sigma=10$ and

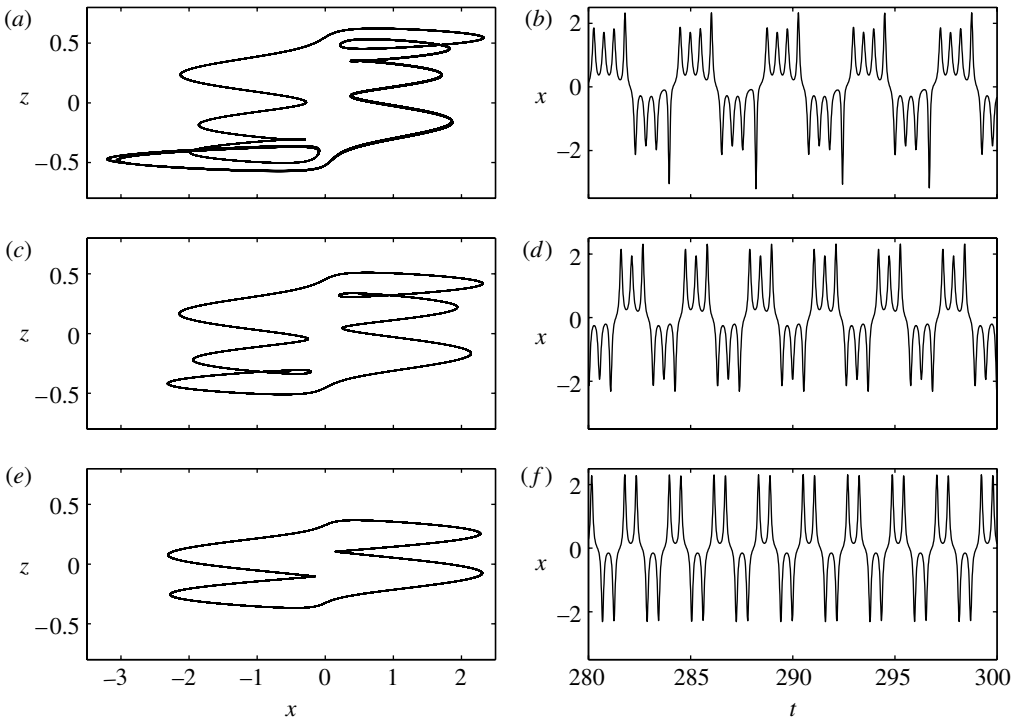

Figure 8. Phase portraits and time-series for $\alpha=100$, $\lambda=1.2$ and $\kappa=1$. Plots (*a*) and (*b*) $\beta=3.54$; (*c*) and (*d*) $\beta=4.2$; and (*e*) and (*f*) $\beta=4.8$.

$b=8/3$. While the Lorenz plot shows evidence of a single discontinuous cusp, in contrast, the HSA plots possess at least three separate main cusps, together with other discontinous curves. The differences between the two nonlinear models, HSA and Lorenz, may be due to stronger contraction in the Lorenz dynamics. In work to be reported elsewhere, we repeated the same integrations for the four mode EMR dynamo, which has as its limit the Lorenz equations when $\beta\to 0$. The single cusp in the Lorenz case was observed to separate into multiple cusps as β was increased.

Figures 12 and 13 show examples of the lowest order UPO, RL (period of 2.581 s) as well as the period-4 R_2L_2 UPO (period of 4.899 s), and two different period-6 UPOs, L_3R_3 (period of 7.352 s) and LRL_2R_2 (period of 7.56 s). To see how the period of the lowest order UPOs varies with β, we repeated our calculations for three different values of β. Firstly, we chose $\beta=1.3$, which corresponds to a value just beyond the onset of oscillatory solutions. Unlike the $\beta=2$ case, we found very few instances of the period-2 RL cycle. Instead, the dominant UPO was the R_2L_2 orbit, with period 5.384 s, a value greater than for $\beta=2$. Next, we chose $\beta=2.6$, which lies just before the loss of stability to a periodic solution at $\beta\approx 2.665$. The RL orbit predominates, with a period of ≈ 2.45 s. Finally, we computed the period of the stable period-2 RL cycle beyond the chaotic regime for $\beta=2.7$ and found its period to be 2.4056 s. Thus, as β increases, the period of the dominant

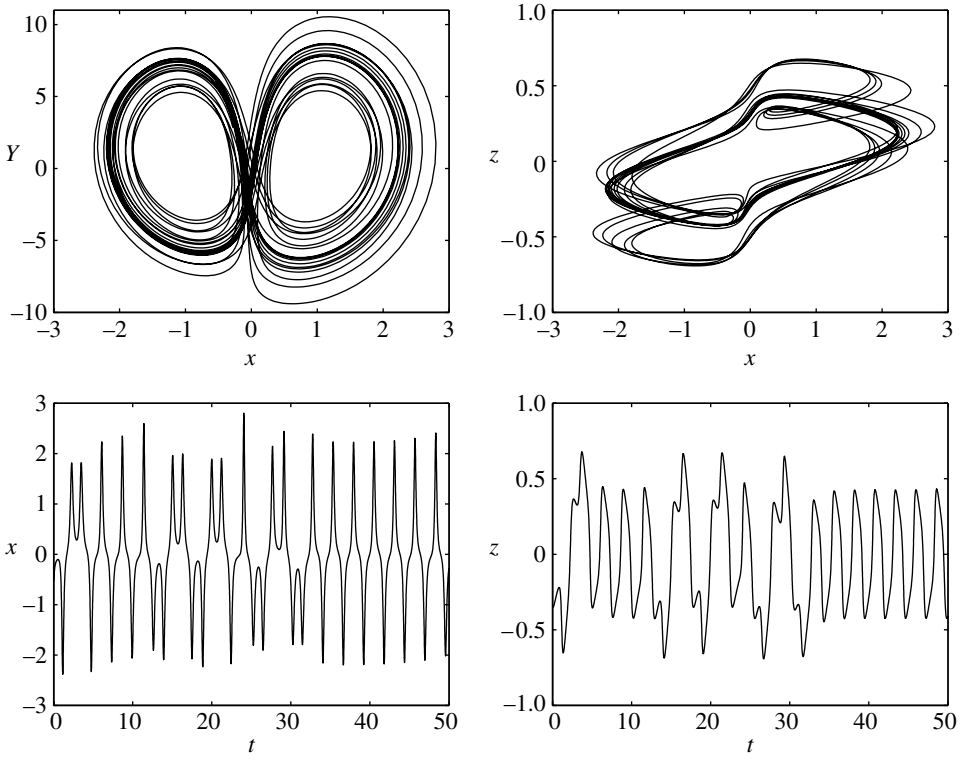

Figure 9. Phase portraits and time-series for $\alpha=20$, $\beta=2$, $\lambda=1.2$ and $\kappa=1.0$.

lowest order UPO decreases. Since β measures the inverse moment of inertia of the armature of the motor, increasing β means reducing rotational inertia, enabling the frequency of oscillation to increase.

(*d*) $\alpha=100$

When $\alpha=100$, we chose $\beta=1.11$, $\lambda=1.2$ and $\kappa=1$ as producing time-series and phase portraits as close as possible to those of figure 9*b* of HSA, while not being degenerate in the sense of §2*a*. Figure 14 shows plots of $x(t)$ and $z(t)$ for these parameter choices as well as two-dimensional projections in the (x, y) and the (x, z) planes.

Unlike the $\alpha=20$ case, the trajectory spends substantially longer in the vicinity of each finite amplitude equilibrium state, before undergoing a reversal. Figure 15 shows an example of the lowest order period-1 UPO for this case.

To see what happens to the time-series and the phase portraits as we increase β, we integrated the HSA dynamo equations for $\alpha=100$, $\lambda=1.2$, $\kappa=1$ and selected values of β. When $\beta=2$, we obtain the scenario shown in figure 16. The long periods between reversals are considerably shortened in terms of cycles before reversals. Figure 17 shows examples of the period-8 R_4L_4 and period-10 R_3L_3 cycles, with periods 4.489 and 5.436 s, respectively.

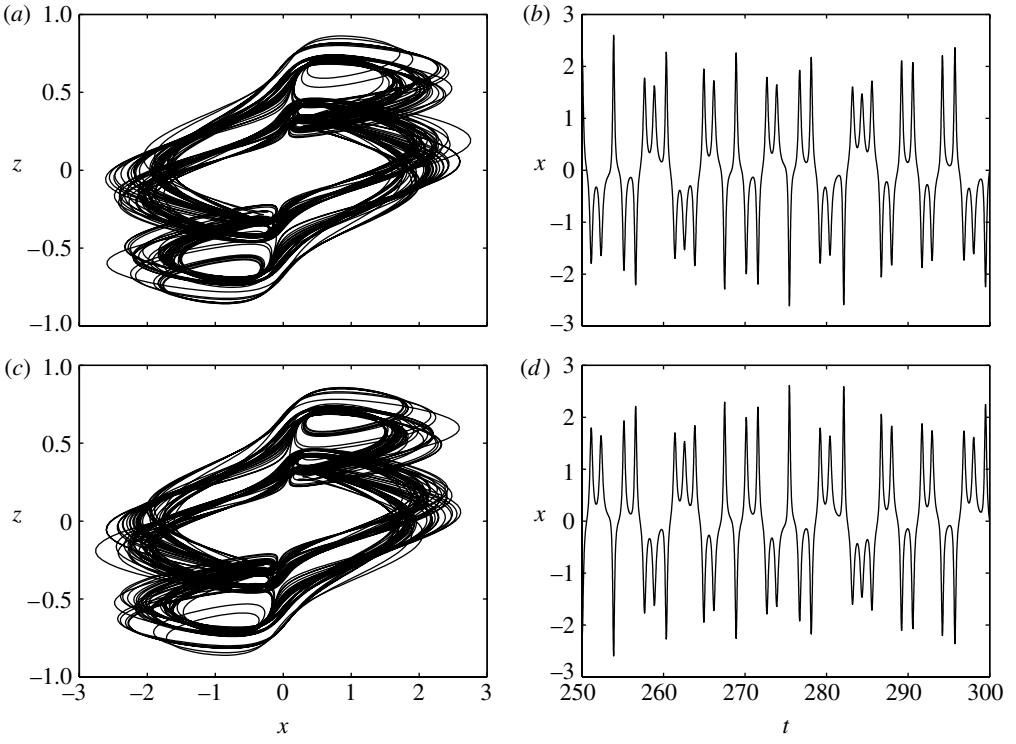

Figure 10. Phase portraits and time-series for $\alpha=20$, $\beta=2$, $\lambda=1.2$ and $\kappa=1.0$ for two different initial conditions (x, y, z) and $(-x, y, -z)$.

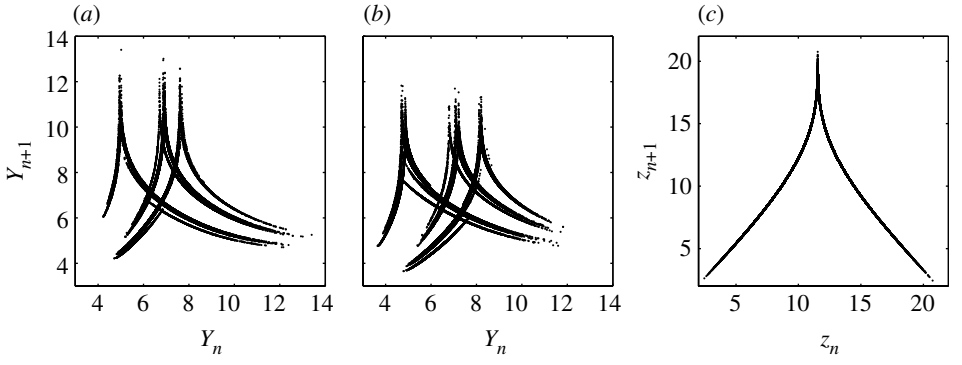

Figure 11. The first return maps as plots of successive maxima of (*a*) Y for $\alpha=20$, $\beta=2$, $\lambda=1.2$ and $\kappa=1.0$; (*b*) Y for $\alpha=20$, $\beta=2$, $\lambda=1.0$ and $\kappa=1.2$; and (*c*) of z in the Lorenz equations for $r=28$, $\sigma=10$, $b=8/3$.

5. Discussion

One of the main objectives of this study was to return to the original dynamo analysis of HSA and to place some of the results described in that paper into context. We focused upon the two irregular oscillatory examples presented in

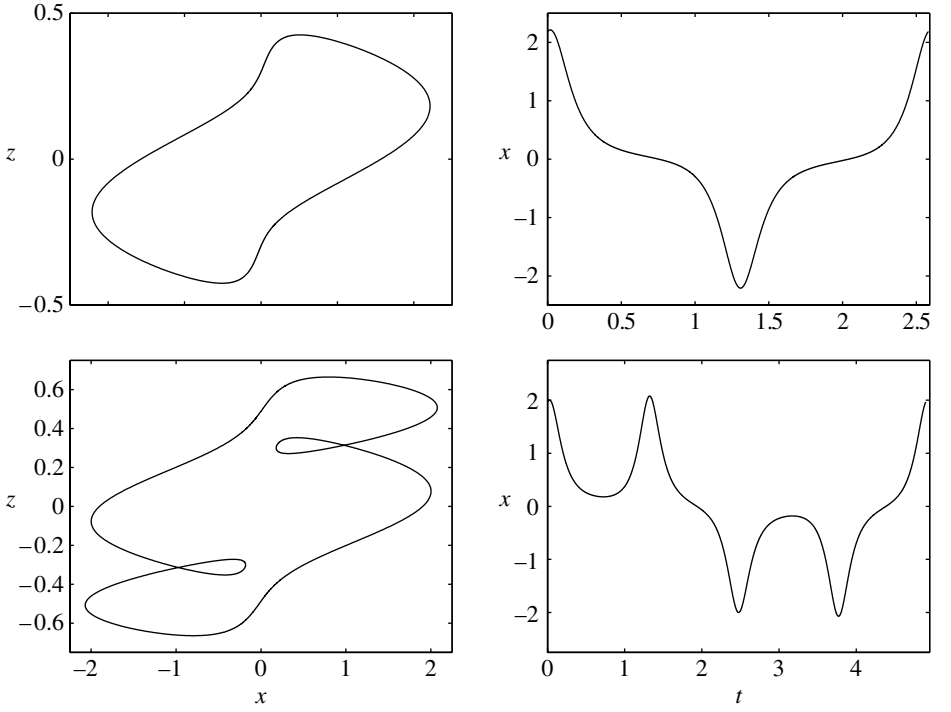

Figure 12. Phase portraits and time-series for one cycle for the RL and R_2L_2 UPOs for $\alpha=20$, $\bar{\beta}=2$, $\lambda=1.2$ and $\kappa=1.0$. The RL UPO shown has a period of 2.581 s, while the R_2L_2 has a period of 4.899 s.

figure 9 of HSA. With the aid of bifurcation transition diagrams, we were able to determine which behaviours could be found in the neighbourhoods of these two parameter choices.

α is a dimensionless measure of the magnitude of the applied couple that drives the disk into rotation, while κ is a dimensionless measure of the mechanical friction in the disk. The HSA remarked that their system fails to function as a self-exciting dynamo, if α/κ is not large enough for motional inductance to overcome ohmic dissipation. In our integrations, we have fixed κ at either $\kappa=1$ or 1.2.

For the $\alpha/\kappa=20$ cases, the driving couple is unable to sustain prolonged oscillations before reversals occur, for values of β/λ slightly larger than at the transition boundary to steady-state solutions.

When $\alpha/\kappa=100$, however, the applied couple is much larger and more sustained irregular oscillations are possible before reversals occur near this loss to steady dynamo states. As β increases, the number of oscillations before reversal decreases until it becomes comparable to the low α/κ cases (see figures 14 and 16). β measures the inverse moment of inertia of the armature and λ, the mechanical friction in the motor. Therefore, small values of β/λ indicate a greater rotational stiffness and lead to a suppression of oscillatory dynamo action.

Hysteresis, and the coexistence of different types of solutions, is a key feature of the HSA model. Depending upon the choice of parameters, coexisting irregular and regular states are possible (e.g. figure 6) as well as different types of periodic

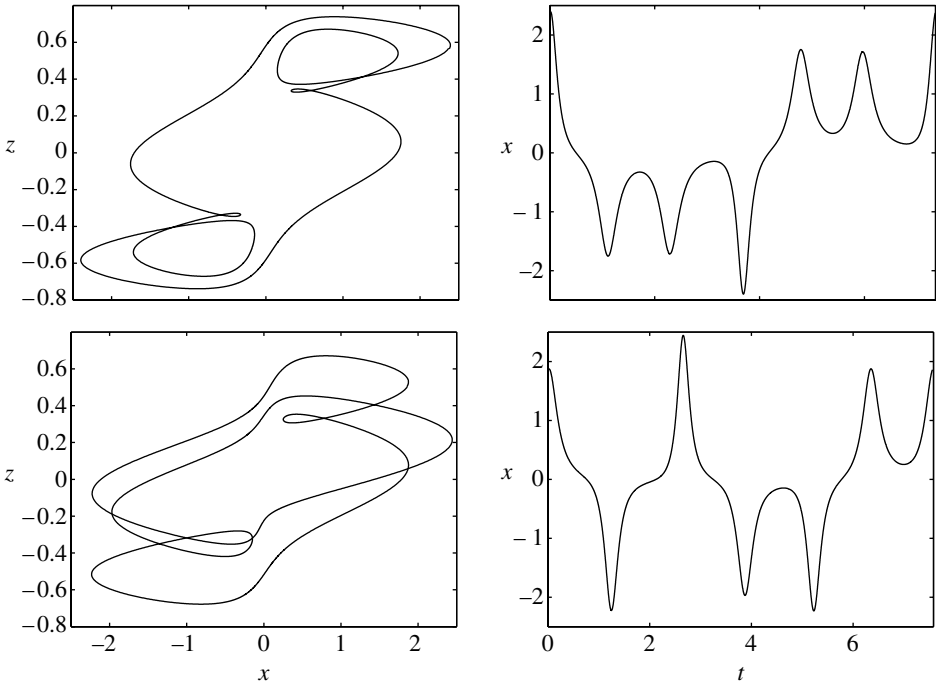

Figure 13. Phase portraits and time-series for one cycle of two different period-6 UPOs. The L_3R_3 UPO in the upper plots has a period of 7.352 s, while the LRL_2R_2 UPO of the lower plots has a period of 7.56 s.

states (see figure 7). We also performed numerical integrations, not reported here, to test the sensitivity of the large-scale and fine-scale structure to changes in incremental step size and initial conditions, for both $\alpha = 20$ and 100. The main differences were found in the periodic regions, after the loss of irregular oscillations, suggesting the coexistence of different stable periodic states as well as the ones reported.

Another objective was to determine the lowest order unstable periodic orbits, responsible for creating some of the irregular behaviour. Our investigations showed that as β increases, the period of the lowest order UPOs decreases. Our analysis, focusing only upon the selected parameter values of $\alpha = 20$ and 100, chosen by HSA for their figure 9, has clearly just scratched the surface regarding the full range of behaviours capable of being supported by the HSA system for other values of α, κ and λ.

The richness of behaviour found in a simpler system, such as the Lorenz equations, which has only three parameters, only one of which is usually varied, has required the efforts of many scientists and papers to understand its possibilities. The HSA dynamo is still relatively unknown in the dynamical systems community. A complete understanding of its potential is also likely to require a number of in-depth studies, of which the present paper is one contribution, in order to elucidate the full range of its behaviours before one can realistically assess the consequences of additional effects, such as azimuthal eddy currents (Hide & Moroz 1999), a nonlinear series motor (Moroz 2002).

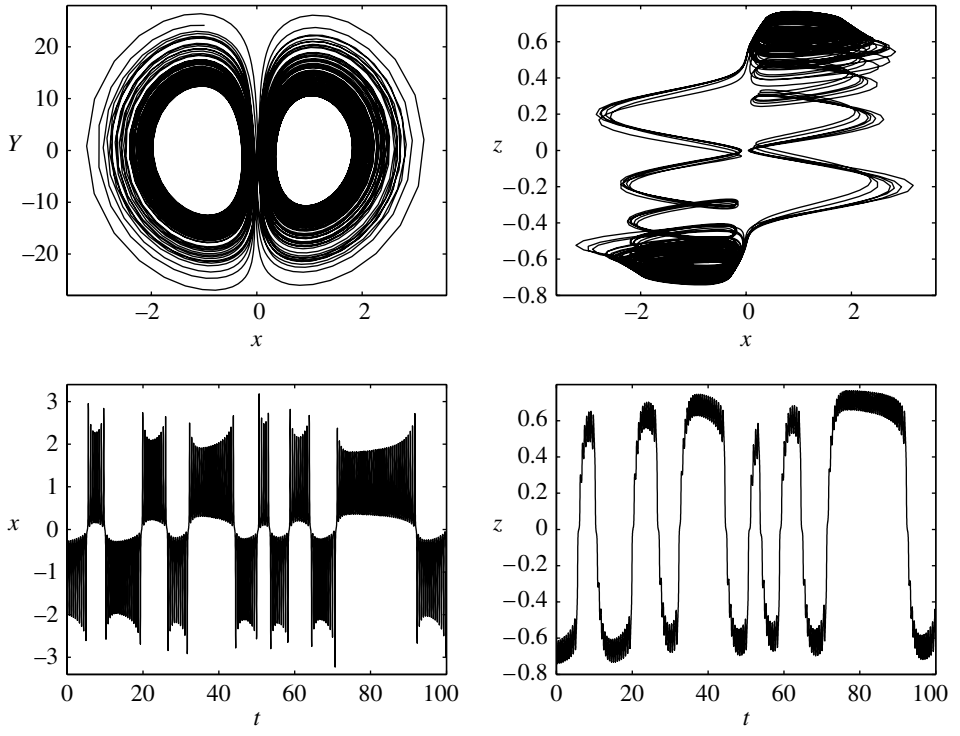

Figure 14. Phase portraits and time-series for $\alpha=100$, $\beta=1.11$, $\lambda=1.2$ and $\kappa=1.0$.

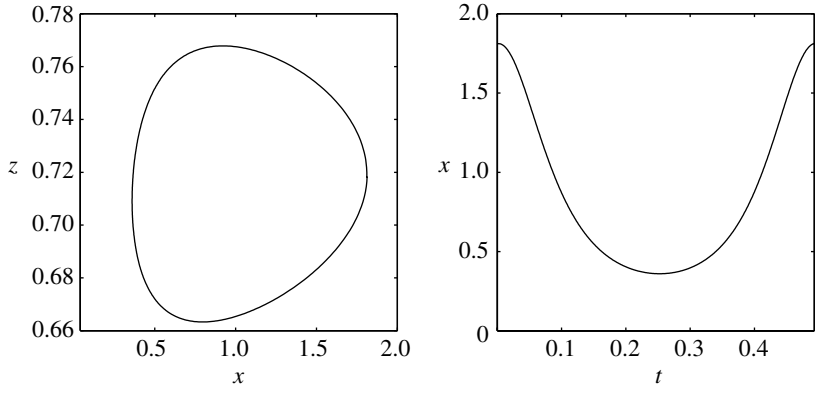

Figure 15. Phase portraits and time-series for the period-1 cycle for $\alpha=100$, $\beta=1.11$, $\lambda=1.2$ and $\kappa=1.0$. The *RL* UPO shown has a period of 0.493 s.

As a first step towards this goal, we have succeeded in placing the behaviours shown in figure 9*a*,*b* of HSA into the context of neighbouring dynamics in parameter space.

The future work will also return to the UPO issue, and address an analysis of the topological structure of the template for the HSA attractor, using ideas developed by Gilmore (1998).

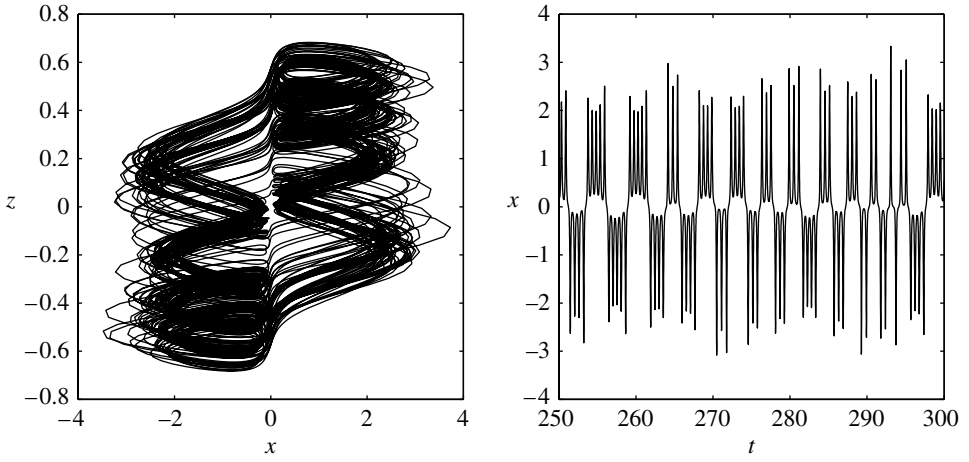

Figure 16. The (x, z)-phase portrait and the x time-series for $\alpha=100$, $\beta=2.0$, $\lambda=1.2$ and $\kappa=1.0$.

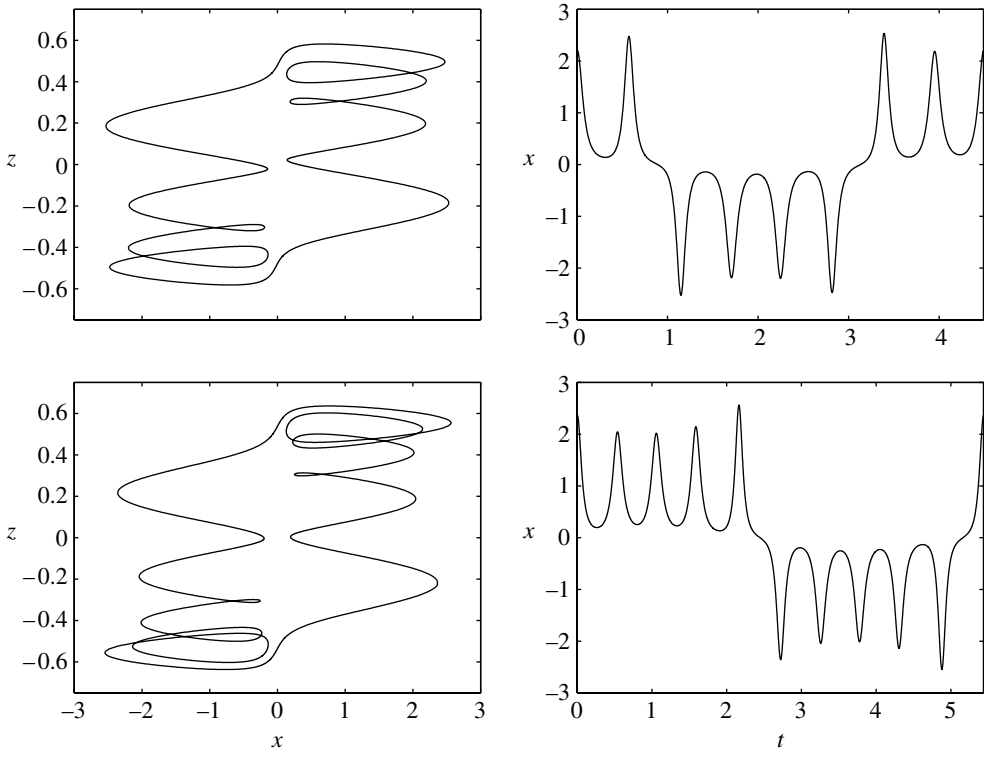

Figure 17. Phase portraits and time-series for one cycle of a period-8 and a period-10 UPO for $\alpha=100$, $\beta=2.0$, $\lambda=1.2$ and $\kappa=1.0$. The R_4L_4 UPO shown has a period of 4.489 s, while the R_3L_3 UPO shown has a period of 5.436 s.

The author is grateful to the anonymous referees for their helpful comments and suggestions, which have clarified and so have helped to improve the quality and understanding of the material presented here.

References

Artuso, R., Aurell, E. & Cvitanovic, P. 1990*a* Recycling of strange sets: I. Cycle expansions. *Nonlinearity* **3**, 325–359. (doi:10.1088/0951-7715/3/2/005)

Artuso, R., Aurell, E. & Cvitanovic, P. 1990*a* Recycling of strange sets: II. Applications. *Nonlinearity* **3**, 361–386. (doi:10.1088/0951-7715/3/2/006)

Gilmore, R. 1998 Topological analysis of chaotic dynamical systems. *Rev. Mod. Phys.* **70**, 1455–1530. (doi:10.1103/RevModPhys.70.1455)

Gilmore, R. & Lefranc, M. 2002 *The topology of chaos, Alice in stretch and Squeezeland*. New York, NY: Wiley.

Goldbrum, P., Moroz, I. M. & Hide, R. 2000 On the biasing effect of a battery on a self-exciting Faraday disk homopolar dynamo loaded with a linear series motor. *Int. J. Bifurcat. Chaos* **10**, 1875–1885. (doi:10.1142/S0218127400001146)

Hénon, M. 1982 On the numerical computation of Poincaré maps. *Physica D* **5**, 412–414. (doi:10.1016/0167-2789(82)90034-3)

Hide, R. 1997*a* Nonlinear quenching of current fluctuations in a self-exciting homopolar dynamo. *Nonlin. Process. Geophys.* **4**, 201–205.

Hide, R. 1997*b* The nonlinear differential equations governing a hierarchy of self-exciting coupled Faraday-disk homopolar dynamos. *Phys. Earth Plan. Int.* **103**, 281–291. (doi:10.1016/S0031-9201(97)00038-1)

Hide, R. & Moroz, I. M. 1999 Effects due to induced azimuthal eddy currents in the self-exciting Faraday disk homopolar dynamo with a nonlinear series motor: I. Two special cases. *Physica D* **134**, 287–301. (doi:10.1016/S0167-2789(99)00107-4)

Hide, R., Skeldon, A. C. & Acheson, D. J. 1996 A study of two novel self-exciting single-disk homopolar dynamos: theory. *Proc. R. Soc. A* **452**, 1369–1395.

Koga, S. 1986 Phase description method to time averages in the Lorenz system. *Prog. Theor. Phys.* **76**, 335–355. (doi:10.1143/PTP.76.335)

Lorenz, E. N. 1963 Deterministic non-periodic flow. *J. Atmos. Sci.* **20**, 130–141. (doi:10.1175/1520-0469(1963)020<0130:DNF>2.0.CO;2)

Moroz, I. M. 2001*a* On the behaviour of a self-exciting Faraday disk homopolar dynamo with battery in the presence of an external magnetic field. *Int. J. Bifurcat. Chaos* **11**, 1695–1705. (doi:10.1142/S0218127401002948)

Moroz, I. M. 2001*b* Self-exciting Faraday disk homopolar dynamos. *Int. J. Bifurcat. Chaos* **11**, 2961–2975. (doi:10.1142/S0218127401004017)

Moroz, I. M. 2002 On the behaviour of a self-exciting Faraday disk homopolar dynamo with a variable nonlinear series motor. *Int. J. Bifurcat. Chaos* **12**, 2123–2135. (doi:10.1142/S0218127402005728)

Moroz, I. M. 2003 The Malkus–Robbins dynamo with a linear series motor. *Int. J. Bifurcat. Chaos* **13**, 147–161. (doi:10.1142/S0218127403006431)

Moroz, I. M. 2004 The Malkus–Robbins dynamo with a nonlinear motor. *Int. J. Bifurcat. Chaos* **14**, 2885–2892. (doi:10.1142/S0218127404010928)

Moroz, I. M. 2005*a* The extended Malkus–Robbins dynamo as a perturbed Lorenz system. *Nonlin. Dynam.* **41**, 191–210. (doi:10.1007/s11071-005-2808-x)

Moroz, I. M. 2005*b* Unstable periodic orbits of the perturbed Lorenz equations. In ENOC-2005, Eindhoven, Netherlands, 7–12 August 2005, pp. 886–890.

Moroz, I. M., Hide, R. & Soward, A. M. 1998 On self-exciting coupled Faraday disk homopolar dynamos driving series motors. *Physica D* **117**, 128–144. (doi:10.1016/S0167-2789(97)00305-9)